

A spectroscopic inference and SOLPS-ITER comparison of flux-resolved edge plasma parameters in detachment experiments on TCV

A. Perek^{a,b}, M. Wensing^b, K. Verhaegh^c, B.L. Linehan^d, H. Reimerdes^b, C. Bowman^e, M. van Berkel^a, I.G.J. Classen^a, B.P. Duval^b, O. Février^b, J.T.W. Koenders^{a,f}, T. Ravensbergen^g, C. Theiler^b, M.R. de Baar^{a,f}, MST1 team¹ and the TCV team²

^aDutch Institute for Fundamental Energy Research, De Zaale 20, 5612 AJ Eindhoven, The Netherlands

^bEcole Polytechnique Fédérale de Lausanne (EPFL), Swiss Plasma Center (SPC), CH-1015 Lausanne, Switzerland

^cCCFE, Culham Science Centre, Abingdon, Oxon, OX14 3DB, United Kingdom

^dMassachusetts Institute of Technology, 77 Massachusetts Avenue, NW17 Cambridge, MA 02139, U.S.A

^eYork Plasma Institute, Department of Physics, University of York, Heslington, York YO10 5DD, United Kingdom

^fEindhoven University of Technology, 5612 AZ, Eindhoven, the Netherlands

^gITER Organisation, Route de Vinon-sur-Verdon, CS 90 046, 13067 St. Paul Lez Durance Cedex, France

¹See author list of B. Labit et al. 2019 Nucl. Fusion 59 086020

²See author list of S. Coda et al. 2019 Nucl. Fusion 59 112023

E-mail: artur.perek@epfl.ch

Abstract.

This work presents the use of a collisional-radiative model to infer plasma parameters from 2D emissivities of several deuterium Balmer lines. The emissivities were obtained by MANTIS, an absolutely calibrated, 10-camera imaging polychromator with < 5 mm spatial resolution, up to 800 Hz frame rate, viewing the lower divertor tangentially.

Our analysis of those image frames generates 2D maps of plasma parameters such as electron density, temperature, neutral atomic density and the reaction rates for ionisation, recombination and charge exchange as a function of time. The analysis is compared and validated against a SOLPS-ITER simulation accounting for drifts. The results are compared against the simulation in 2D, radial and poloidal profiles to probe the numerous effects of particle transport in the Scrape-Off Layer, in particular in the approach to detached divertor leg conditions.

The inferred inner divertor leg radial profiles of the electron density and temperature were consistent with the SOLPS-ITER predictions. A significant transport of particles to the private flux region is found experimentally, that is not captured in the simulation. The simulation diverges from the experiment at the outer divertor target, where the plasma emission appears to be consistent with the emission driven by plasma-molecule interactions. Our analysis also shows prospects for aiding the power exhaust control efforts by potentially providing an optical tracking of the particle balance in the divertor.

Keywords: detachment, transport, 2D spectroscopy, marfe, SOLPS-ITER

1. Introduction

Rapid deployment of nuclear fusion as a commercial energy source requires a reactor design that minimises the cost and construction time [1]; this could be achieved through a compact reactor design that could be quickly built and mass-produced. However, design considerations for a compact tokamak reactor inevitably require a high toroidal magnetic field to increase the energy density while decreasing the plasma volume [2]. Such a combination poses a challenge to the power exhaust design for which the engineering challenges scale unfavourably with both increasing magnetic field and decreasing volume [3]. To predict the performance of power exhaust designs, one needs predictive models that are continuously tested against experiments on existing machines.

At the Tokamak à Configuration Variable (TCV), 2D plasma models were compared with Langmuir probe measurements explaining the inner target asymmetry [4]. Simulations also matched the results of the alternative divertor geometry experiments [5] and were used to predict the effects of different divertor closure designs [6]. Validated simulation results can then be used to validate spectroscopic techniques before their application to experimental data [7, 8]. Recently, a novel inference of the particle balance [7] indicated the mechanism behind the ion target current limitation that led to the target particle flux rollover [7, 9]. The target particle flux rollover itself is one of the key indicators of detachment, a regime where heat and particle fluxes to the target are reduced. Detachment is currently thought to be necessary for future high power devices as a viable regime for prolonged operation for the power exhaust [10, 11, 12].

Recently at TCV, a set of divertor baffles was installed to study the effects of the divertor closure on detachment [13, 14, 15, 16]. As a result, a deeper, earlier and symmetric rollover of the ion target current in both targets was observed [14, 16]. However, in contrast to the experiment, rollover of the target ion fluxes is not obtained in the corresponding SOLPS-ITER simulations [17, 18]. Simulations did, however, predict an X-point potential well that was subsequently verified experimentally with the Reciprocating Divertor Probe Array [19, 20]. Furthermore, in the simulation, the X-point potential well induces an ExB drift which is expected to be a dominant radial particle transport mechanism [19].

The aim of this paper is to determine whether the plasma parameters are accurately reproduced in SOLPS-ITER. Investigating the accuracy of this match can provide information on how accurately the cross-field particle transport is captured in SOLPS-ITER.

This paper also presents the development and validation of a 2D analysis technique of the Balmer line emission to infer flux-resolved hydrogenic power and particle balance from imaging data. Quantitative analysis of 2D imaging data is currently pursued on European tokamaks. A similar analysis [21] was recently applied at JET using a four-channel imaging system [22] to assess the particle balance in the divertor [23]. At MAST-U, a 2D inference is being developed to infer plasma parameters directly from absolutely calibrated images [8].

These aims are achieved by inferring the electron density, temperature, neutral atomic density and the reaction rates for ionisation and recombination together with their respective power loss rates in the form of 2D maps from measurements of the deuterium Balmer line emissivities using the MANTIS system [24, 25]. The analysis technique and the underlying assumptions are presented in section 2. In section 3, the experimental scenario and the simulation setup are described. Then, by employing similar upstream electron density and temperature conditions, inferred

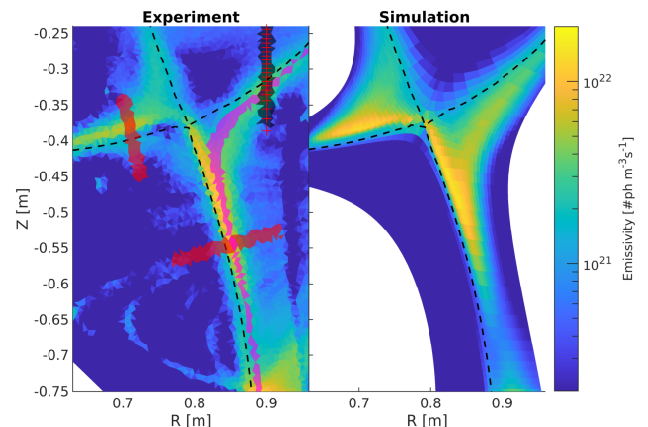


Figure 1. Emissivity of the $D_{3\rightarrow 2}$ line measured by MANTIS and predicted by SOLPS-ITER with the following inversion cell markers: black for cells used in the upstream comparison; red crosses for the Thomson Scattering locations; red cells for the radial profiles on inner and outer divertor legs; magenta cells for the poloidal profile. TCV #63546, $t = 1.115$ s; SOLPS-ITER #150141.

neutral atomic density and the ionisation rate are compared. Next, the upstream plasma conditions are used to determine suitable parameter ranges to perform the analysis on the 2D emissivity data, in section 4. Then, the resulting maps are compared to the SOLPS-ITER predictions in detailed 1D profiles at locations marked in Figure 1. The simulation results are used to generate synthetic analysis data based on known plasma parameters as input to the ADAS model to verify the implementation and validate the analysis method itself. The synthetic data analysis results are presented in sections 4 and 5.

Section 5 presents the ion sources in a flux-resolved comparison against the Langmuir probe measurements and SOLPS-ITER predictions. Finally, in section 6, the formation and the investigation of the physics behind a High Field Side (HFS) MARFE is presented. The time traces of chosen plasma parameters are shown, highlighting the role of the MARFE and the upstream pressure loss in the ion target current reduction. This section also compares the inferred peak and total ion target currents against the Langmuir probe data, demonstrating this technique's potential for power exhaust control efforts by potentially providing optical tracking of the particle flux to the divertor target.

2. Analysis method

In this section, the Bayesian inference is used to compare measured Balmer emissivity of deuterium with a plasma emission model to obtain a Probability Density Function (PDF) of the electron density, temperature and neutral atomic density. The second part of this section describes how the PDF is processed to obtain: the electron density, temperature, neutral atomic density, the reaction rates for ionisation, recombination and charge exchange, together with the power loss rates for ionisation and recombination. In the third part, variations of this technique, including additional information, are described.

2.1. Generation of the Probability Density Function

The Balmer line emission with a quantum number n is the sum of excitation and recombination contributions. These parts can be modeled using Photon Emissivity Coefficients $PEC_{n \rightarrow 2}^{rec, exc}$ obtained from the ADAS collisional-radiative model [26]. The total brightness can be written as:

$$B_{n \rightarrow 2} = n_i n_e PEC_{n \rightarrow 2}^{rec}(n_e, T_e) + n_o n_e PEC_{n \rightarrow 2}^{exc}(n_e, T_e) \quad (1)$$

where n_o is the hydrogen atomic neutral density. The ADAS model assumes that: the emission comes from plasma volume with a constant n_e and T_e , the model is valid for deuterium, $Z_{eff} = 1$ and

that the contributions from molecular reactions are negligible. In principle, Z_{eff} could play a role in the recombination contribution. However, recombination emission is promoted in the regions of low T_e , insufficient to maintain high Z_{eff} . The validity of the last assumption can be questionable in the divertor where the plasma-molecule interaction can be a significant source of the $D_{3 \rightarrow 2}$ emission [27, 28]. The possibility of molecular contributions will be investigated later in this paper. In the case of upstream conditions, relatively low density, $n_e \approx 2 \cdot 10^{19} \text{ m}^{-3}$ combined with $T_e > 5 \text{ eV}$, are unfavourable for the Molecularly Activated Recombination (MAR) that leads to such emission [29].

Assuming $n_i = n_e$, equation 1 can be used to construct a system of equations describing the plasma emission across the deuterium Balmer lines for $n = 3, 4, 5$:

$$\begin{cases} B_{3 \rightarrow 2} = n_e^2 PEC_{3 \rightarrow 2}^{rec}(n_e, T_e) + n_o n_e PEC_{3 \rightarrow 2}^{exc}(n_e, T_e) \\ B_{4 \rightarrow 2} = n_e^2 PEC_{4 \rightarrow 2}^{rec}(n_e, T_e) + n_o n_e PEC_{4 \rightarrow 2}^{exc}(n_e, T_e) \\ B_{5 \rightarrow 2} = n_e^2 PEC_{5 \rightarrow 2}^{rec}(n_e, T_e) + n_o n_e PEC_{5 \rightarrow 2}^{exc}(n_e, T_e) \end{cases}$$

In the experiment, n_e , T_e and n_o are the unknowns while $B_{3 \rightarrow 2}$, $B_{4 \rightarrow 2}$, $B_{5 \rightarrow 2}$ are measured. To solve this system for n_e , T_e and n_o , the experimentally measured emission will be compared against modeled emission.

For the comparison, a lookup table of modeled brightness, $B_{n \rightarrow 2}^{modelled}(n_e, T_e, n_o)$ was computed using equation 1 for a 20 point per decade grid of logarithmically spaced plasma parameters with T_e ranging from 0.2 eV to 150 eV; n_e in the range $5 \cdot 10^{18} \text{ m}^{-3}$ to $2 \cdot 10^{20} \text{ m}^{-3}$ and the neutral atomic density n_o between 10^{15} m^{-3} and 10^{20} m^{-3} . For numerical stability, the computation is carried out in \log_{10} of all parameters. Next, the emissivity measurements are compared against the modeled values in the lookup table. To determine the likelihood with which n_e , T_e and n_o in the lookup table correspond to the measured emissivity, each lookup table cell is assigned a likelihood value describing the goodness of the fit as:

$$P_{B_{n \rightarrow 2}}(n_e, T_e, n_o) \propto e^{-\left(\frac{B_{n \rightarrow 2}^{modelled} - B_{n \rightarrow 2}^{measured}}{B_{n \rightarrow 2}^{err}}$$

This function assumes a normal distribution of probability. It is the highest when the measured and modelled values match and exponentially decays as they deviate from each other. The uncertainty, $B_{n \rightarrow 2}^{err}$, derived from the tomographic inversion and the absolute calibration, defines the decay rate [24]. Together, those likelihoods form a probability density function (PDF) of fitting one Balmer line.

The next step is to combine the probabilities for each Balmer line as a product which gives the PDF of

matching all included lines simultaneously:

$$P(n_e, T_e, n_o) = P_{B_{3 \rightarrow 2}} P_{B_{4 \rightarrow 2}} P_{B_{5 \rightarrow 2}}. \quad (3)$$

The PDF can be further supplemented with additional information. The $B_{7 \rightarrow 2}$ is also experimentally measured in with MANTIS. However, as shown in previous work, this spectral line cannot be easily separated in MANTIS's cavity due to neighbouring impurity lines, $O\ II$ in particular [24]. As a result, the measured brightness of the $B_{7 \rightarrow 2}$ line can only be higher than its actual value. This information was utilized to further constrain the PDF $P_{B_{n \rightarrow 2}}(n_e, T_e, n_o)$ by removing probabilities in the regions of the lookup table for which:

$$B_{7 \rightarrow 2}^{modeled} > B_{7 \rightarrow 2}^{measured} + 3B_{7 \rightarrow 2}^{err}. \quad (4)$$

This procedure is applied to each inversion cell without explicit regularisation, which is applied implicitly in the next step.

One of the difficulties in combining separate camera images is spatial misalignment. An error in the camera calibration can cause an offset between inverted emissivities misplacing the emission gradient, which, in turn, can skew the results. The R, Z location uncertainty was included in the analysis by examining multiple misalignment options when preparing the PDF through a Monte Carlo method. A number of random translations up to 2.5 mm in radial and vertical directions of the poloidal plane are generated for $B_{4 \rightarrow 2}$, $B_{5 \rightarrow 2}$ and $B_{7 \rightarrow 2}$ inversions while $B_{3 \rightarrow 2}$ was kept stationary. Additionally, each node of the inversion grid was translated by $[0.005, -0.005]$ m in the RZ plane to match the strike point locations of the magnetically reconstructed separatrix.

Apart from spacial misalignments, the absolute calibration errors are included by introducing a random offset with a flat distribution of up to 12% to the absolute calibration of each Balmer line individually [24]. This assumes the calibration uncertainties between the various channels are independent.

Then, for each translation, a probability density function, $P_i(n_e, T_e, n_o)$, is generated to obtain the total probability as:

$$P^{tot}(n_e, T_e, n_o) = \frac{1}{m} \sum_{i=1}^m P_i(n_e, T_e, n_o). \quad (5)$$

Testing showed that the $m > 35$ was generally sufficient to converge to a stable probability density function, but $m = 150$ was finally chosen.

To obtain the PDFs for n_e , T_e or n_o ; P^{tot} is marginalized with respect to the other two variables, for example:

$$P^{tot}(n_e) = \int \int P^{tot}(n_e, T_e, n_o) dT_e dn_o. \quad (6)$$

The PDF is then normalised, and the maximum likelihood is determined together with the smallest

interval containing 68% of the probability as the uncertainty estimate.

2.2. Calculation of the plasma parameters

To calculate the plasma parameters, the PDF is represented as a set of samples. The samples are generated with a Monte Carlo distribution as random combinations of n_e , T_e and n_o ; each with a random probability P_{sample} ranging from 0 to the maximum likelihood of the PDF. If $P_{sample} < P^{tot}(n_e, T_e, n_o)$, the sample is kept, else the sample is rejected. As a result, the distribution of samples reflects the PDF.

The samples are used to calculate samples of ionisation, recombination and the charge exchange reaction rates as:

$$I_{rate} = n_e n_o SCD(n_e, T_e), \quad (7)$$

$$R_{rate} = n_i n_e ADC(n_e, T_e) \approx n_e^2 ADC(n_e, T_e), \quad (8)$$

$$CX_{rate} = n_i n_o CCD(n_e, T_e) \approx n_e n_o CCD(n_e, T_e). \quad (9)$$

The SCD , ADC and CCD are their respective rate coefficients obtained from ADAS [26]. Analogically, the power loss rates for ionisation, P^{exc} and recombination, P^{rec} are calculated using their respective rate coefficients: PLT and PRB [26]. The same hold for the inferred brightness of the Balmer lines using equation 1 under the assumption that $n_i = n_e$.

The resulting samples of plasma parameters are processed with a kernel density estimator to approximate their PDFs [30]. The PDF is then normalised, and the maximum likelihood is determined together with the smallest interval containing 68% of the probability as the uncertainty estimate.

2.3. Variations of the analysis method

Equation 6 can be extended with additional information. In the case of the upstream profile comparison, shown in section 3.3, the electron density and temperature are also locally available from Thomson Scattering (TS). Electron density and temperature measurements can be included in the analysis by interpolation of the TS data in the flux space to the cell locations for which $B_{3 \rightarrow 2}^{measured}$ is measured. In this analysis, only the TS measurements below the mid-plane are used. The uncertainty of the measurement location is treated analogically to the emissivity before the interpolation. Finally, a normal distribution of probability is assumed to derive $P_{T_e}^{TS}$ and $P_{n_e}^{TS}$ as:

$$P_{T_e}^{TS}(n_e, T_e, n_o) \propto e^{-\left(\frac{T_e^{modelled} - T_e^{measured}}{2T_e^{err}}\right)^2}, \quad (10)$$

and for the electron density,

$$P_{n_e}^{TS}(n_e, T_e, n_o) \propto e^{-\left(\frac{n_e^{modelled} - n_e^{measured}}{2n_e^{err}}\right)^2}. \quad (11)$$

The uncertainties T_e^{err} and n_e^{err} correspond to the 95% confidence intervals derived from the Thomson scattering data. The resulting probabilities are included in the product of probabilities in equation 6.

The second option of additional information is the static plasma pressure, $p = 2n_e T_e$. In the divertor, the static pressure should not be higher than the upstream value at the separatrix. This limit will be applied in section 4 to exclude the likelihoods with combinations of n_e and T_e exceeding the upstream plasma pressure by taking a single, conservative upstream value for the entire experiment.

3. Matching simulation and experiment

When comparing SOLPS-ITER simulations to the experimental data, one needs first to consider the upstream profiles. Apart from the plasma density, temperature and composition, the optical emission also depends on the neutral atomic density. The neutrals play an essential role at the plasma edge by undergoing ionisation and charge exchange reactions leading to power and momentum losses from the plasma. Neutral particles can be stored in; and released from the machine walls. On TCV, when sufficient, the neutral pressure can be measured using a set of baratrons. The baratron measurement requires a complex model to interpret the molecular pressure measured by the gauge [6]. The baratrons thus indicate a global pressure, whereas the local plasma-neutral interaction can be affected by the many other components [5, 14, 31]. A recent comparison between SOLPS-ITER and a TCV discharge found a difference between measured and simulated baratron pressure up to a factor 5 [32]. A local measure of the neutral density would thus be more suitable in this comparison. This section presents the experimental scenario, the simulation setup. Then, the variation of the analysis method from section 2.3 is used to obtain the experimental upstream profiles. Those are compared to determine whether the neutral atomic density is well captured by SOLPS-ITER or mismatched as the previous findings would suggest [32].

3.1. Experimental scenario

The experimental data presented in this paper was acquired during an unseeded, ohmic L-mode density ramp discharge at 250 kA in the magnetic field direction unfavourable for H-mode access (∇B drift away from the X-point). This discharge is a portion of a larger study that was carried out in the framework of the European PEX (Plasma EXhaust) program [14, 16]. As the line averaged density increases in this scenario, the divertor target cools to below temperatures for efficient excitation of hydrogen,

$\lesssim 4$ eV, which approximately coincides with the ionisation front. This behaviour can be observed in both the simulation and the experiment, which serves as a qualitative matching parameter that narrows the search for the upstream profiles match. The discharge was recorded with the MANTIS system [25] containing a filter set with Balmer $D_{3\rightarrow 2}$, $D_{4\rightarrow 2}$, $D_{5\rightarrow 2}$, $D_{7\rightarrow 2}$, which are also referred to as D_α , D_β , D_γ and D_ϵ respectively in this paper. The C III triplet centered 465 nm was also measured. The absolute calibration and the tomographic inversion process, together with the important interference filter characteristics, are described in [24].

3.2. Simulation setup

SOLPS-ITER simulations based on an identical magnetic equilibrium (TCV #62807, $t = 1.0$ s) and including vessel geometry with gas baffles are used. An extensive discussion on the simulation for settings used in our TCV simulations are provided in [6, 20]. The simulations shown here are obtained with a fixed heating power of 330 kW, assumed equally distributed between electrons and ions, yielding a $P_{SOL} \approx 300$ kW comparable to the experimentally inferred value. Neutrals are treated kinetically by coupling to Eirene code. The plasma density is scanned by varying of the D_2 -gas puff rate, corresponding to $6 - 40 \cdot 10^{21} D_0/s$ from a source at the location on the floor at $R = 0.88$ m. Drifts and currents are included in these simulations and found to significantly influence the divertor particle transport [19], consistent with simulation results on other machines e.g. DIII-D [33] and ASDEX Upgrade [34, 35, 36, 37]. In absence of a physics model for turbulent cross-field transport, spatially constant anomalous transport coefficients $D_\perp = 0.2 \text{ m}^2 \text{ s}^{-1}$ and $\chi_{e,i,\perp} = 1.0 \text{ m}^2 \text{ s}^{-1}$ are used to obtain fall-off length $\lambda_n \sim 1.4$ cm, $\lambda_T \sim 1.1$ cm that provide a reasonable match to the experimental upstream profiles obtained from Thomson scattering [32].

3.3. Upstream profile comparison

The results presented in this section were obtained with the analysis method described in the previous section with the inclusion of Thomson Scattering data as described in section 2.3. Figure 2a) shows a comparison between the inferred upstream density and temperature profiles and their modelled counterparts. The main discrepancy is found in the far SOL but remains well within a factor of 2. The decay lengths of the upstream profiles appear to be overestimated by the simulation. The value at the separatrix is well reproduced.

Figure 2b) shows the neutral density comparison.

As most neutral atoms are created via dissociation of molecular hydrogen, they can diffuse either towards the core or at the machine walls. The neutral atoms encounter a sink, either due to ionisation in the plasma or recombination, forming a new molecule at the reactor wall. In the case of TCV, the walls are made of graphite, which has a chemical affinity with hydrogen. The slope towards the core is well reproduced in the simulation. A significant difference is found outside the LCFS, where the simulated neutral density plateaus while the inferred value decreases. This disagreement can be interpreted as a difference in the wall recycling coefficient for neutral atoms. In the simulation, the divertor chamber serves as a neutral reservoir (both

atomic and molecular) that recycle via reflections from the machine walls. In the experiment, locally produced neutral atoms diffuse outwards, appear to be recombined into molecular deuterium, trapped in the walls or lost in other interactions with available species. This would explain the decrease in their density away from the plasma. The proximity to the outer baffle can also play a role in neutral particle pumping. This finding suggests that most neutral atoms at the plasma edge originate from molecules dissociated shortly before ionisation, highlighting the significance of the plasma-molecule interactions.

Figure 2c) compares the ionisation in the SOL that is shifted towards the core in the experiment with respect to the simulation. It could be caused by the difference in the electron and neutral atomic density profiles.

Figure 2d) presents Balmer line emissivities together with the reconstructed and simulated values. The reconstruction matches the measured values except for D_ϵ , which is extrapolated below the measured value. This is consistent with the impurity pollution elevating the measured emissivity.

4. Electron density, temperature and neutral atomic density comparison

The SOLPS-ITER simulations predict a formation of the X-point potential well, which results in a substantially reshaped $E \times B$ -flow pattern for detached divertor conditions [19]. Furthermore, the existence of the potential well was experimentally observed with the use of the Reciprocating Divertor Probe Array

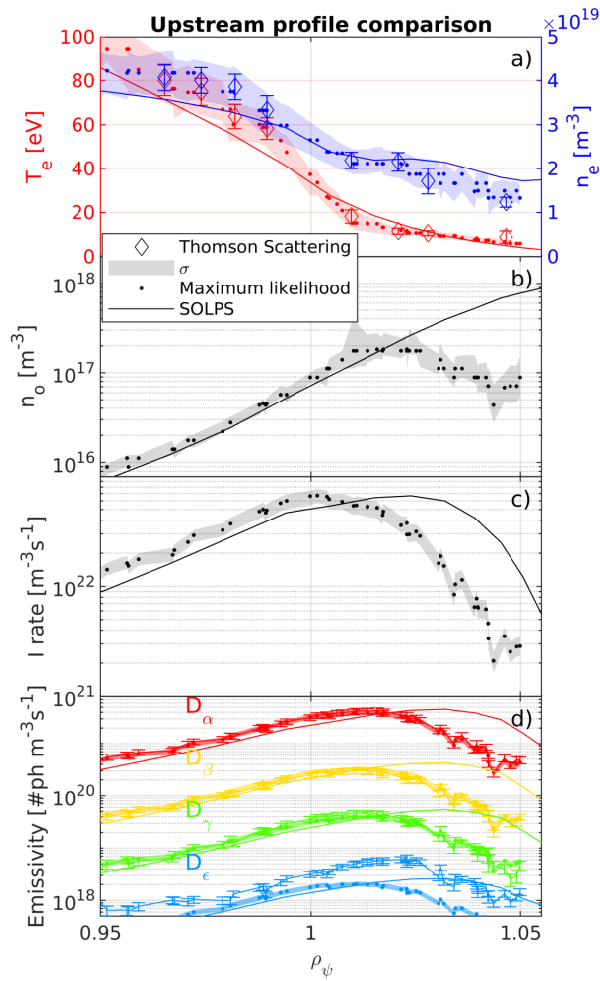


Figure 2. Upstream profiles along the Thomson scattering intersection below the mid-plane: a) Inferred profiles of T_e , n_e together with the SOLPS-ITER simulation equivalent and the Thomson scattering data; b) Inferred neutral density together with the simulation prediction; c) Inferred ionisation rate; d) D_α emissivity together with the reconstructed profile and its simulation prediction. TCV #63546, $t = 1.115$ s; SOLPS-ITER #150141; Location: black cells in Figure 1.

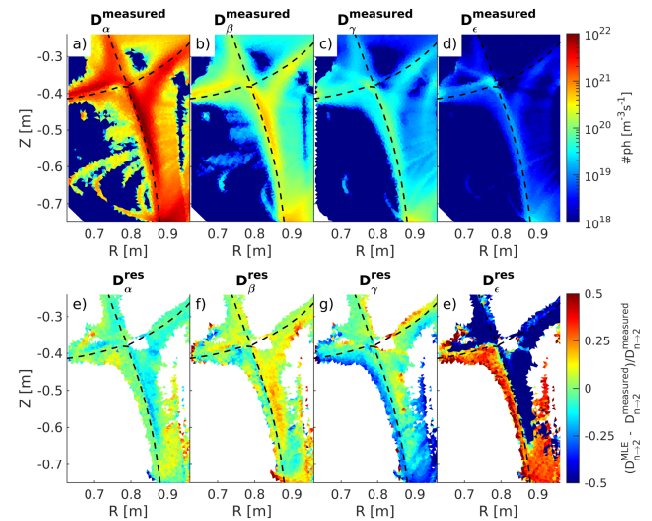


Figure 3. Top row: emissivity of the Balmer series measured in MANTIS. Bottom row: relative difference between the Maximum Likelihood Estimate (MLE) of the reconstructed emissivity and the measured value. TCV #63546, $t = 1.115$ s.

[38, 39]. The resulting radial particle transport is expected to lead to a radial shift between density and temperature profiles on the HFS. This section will compare the inferred density and temperature maps to verify this shift's existence and magnitude.

The analysis ranges were altered to reflect expected divertor parameters with T_e ranging from 0.2 eV to 50 eV; n_e in the range $5 \cdot 10^{18} \text{ m}^{-3}$ to $2 \cdot 10^{20} \text{ m}^{-3}$ and the neutral atomic density n_0 from 10^{16} m^{-3} to $1 \cdot 10^{20} \text{ m}^{-3}$. One additional constrain was added, stating that the predicted static plasma pressure in the SOL cannot exceed its upstream value of $p_u = 480 \text{ Pa}$, as described in section 2.3.

Cells within $\rho_\psi = [0.95, 1.12]$ were analysed and the residuals are shown in Figure 3. The residual values show that the Maximum Likelihood Estimate (MLE) of a vast majority of the inferred cells reproduce measured emissivity within 20%. The exception is found in D_ϵ , which is only used as an additional constrain due to the measured value possibly containing significant contributions from impurity lines [24]. Hence, the reconstructed value of D_ϵ is expected to be lower than measured in the contaminated regions.

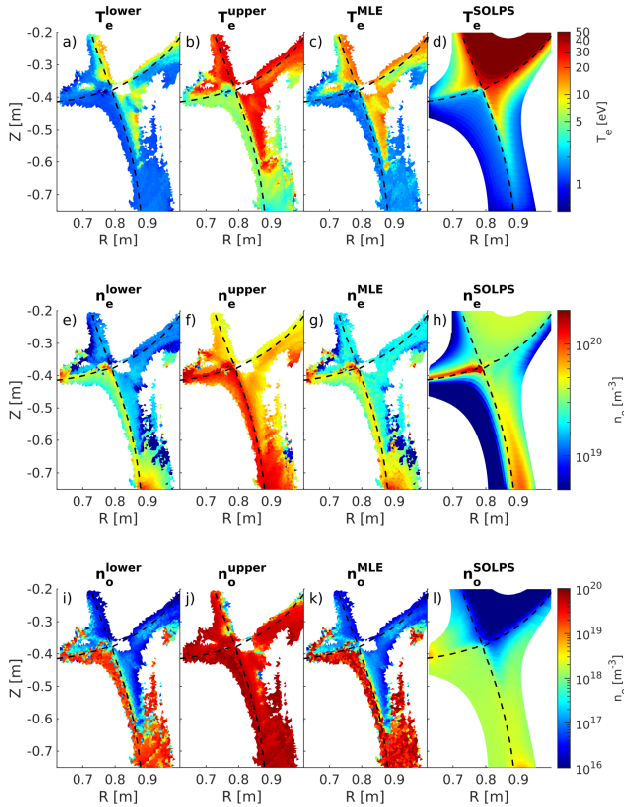


Figure 4. Upper and lower bound of 1σ confidence interval together with the Maximum Likelihood Estimate of the inferred values of plasma density, temperature and atomic hydrogen density and the SOLPS-ITER solution. TCV #63546, $t = 1.115 \text{ s}$; SOLPS-ITER #150141.

Figure 4 shows the analysis results. The lower and upper bound of the 68% confidence intervals indicate the uncertainty range together with the Maximum Likelihood Estimate (MLE). Inferred temperature map decreases monotonically along the divertor leg towards the target. The maps also reveal a region of low T_e and high n_e at the HFS near the X-point captured by SOLPS simulations. This structure is not present in the corresponding simulations with the drifts deactivated [6, 19]. More details can be seen in a 1D radial profile across the inner divertor leg shown in figure 5. The figure shows a comparison between the experimental data analysis, the SOLPS-ITER result and its synthetic data analysis. Figure 5b) shows a radial shift of the n_e profile with respect to the T_e profile in the $v_r^{E \times B}$ -direction (section 7.4.3 of [20]). The figure also contains the analysis run on the synthetic data, which shows that such a shift can be recovered. Figure 5a) shows the analysis results for the experimental data, which produces a similar shift of the n_e profile.

Thus, confirming that the radial emission profiles and subsequently inferred plasma parameters on the HFS are consistent with the simulation results, where the radial transport in the inner divertor leg is predicted

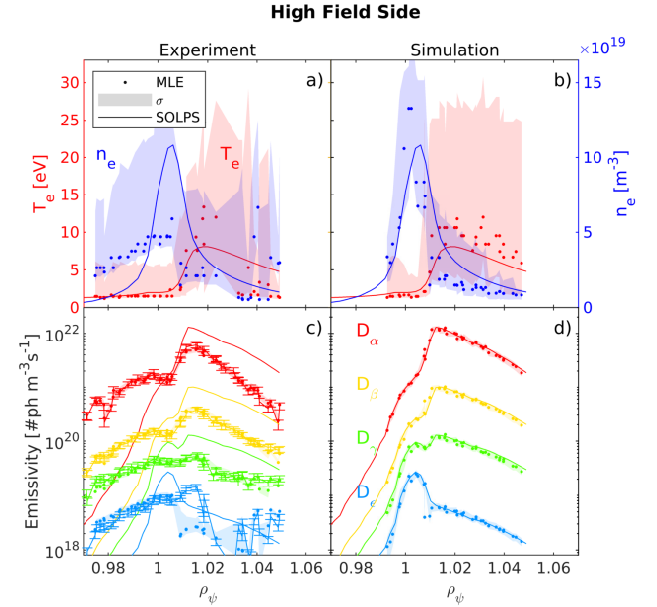


Figure 5. High Field Side radial profiles: a) inferred density and temperature together with the SOLPS-ITER predictions; b) SOLPS prediction together with the synthetic emissivity analysis output; c) experimentally measured emissivity with 68% confidence interval of reconstructed emissivity (shaded regions mostly covered by the error bars) and SOLPS predictions (solid lines); d) emissivities predicted by SOLPS (solid lines) together with the interpolated emissivity for synthetic testing and a 68% confidence interval of reconstructed emissivity. Location: red cells on the HFS in Figure 1. TCV #63546, $t = 1.115 \text{ s}$; SOLPS-ITER #150141.

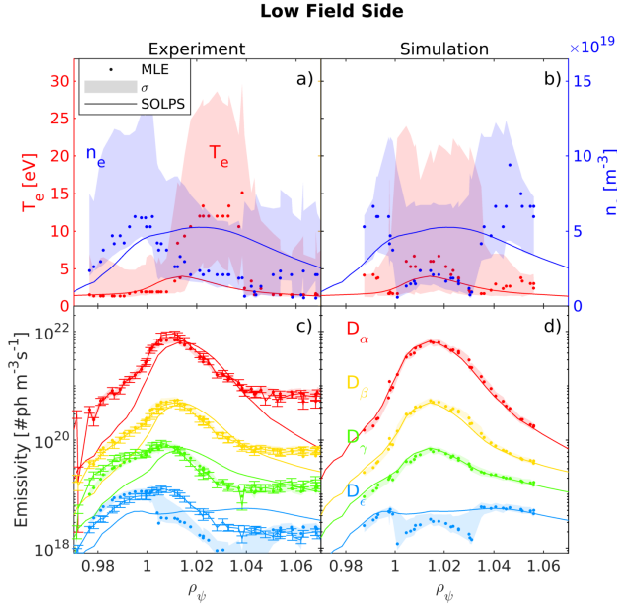


Figure 6. Low Field Side radial profiles: a) inferred density and temperature together with the SOLPS-ITER predictions; b) SOLPS prediction together with the synthetic emissivity analysis output; c) experimentally measured emissivity with 68% confidence interval of reconstructed emissivity (shaded regions mostly covered by the error bars) and SOLPS predictions (solid lines); d) emissivities predicted by SOLPS (solid lines) together with the interpolated emissivity for synthetic testing and a 68% confidence interval of reconstructed emissivity. Location: red cells on the LFS in Figure 1. TCV #63546, $t = 1.115$ s; SOLPS-ITER #150141.

to be $E \times B$ -dominated.

The experimental density profile extends much further to the Private Flux Region (PFR) than the simulated counterpart, with a sharp fall-off at the separatrix. A smooth transition of n_e through the separatrix suggests that the separatrix does not limit the radial transport. This observation shows the existence of a cross-field transport to the PFR region, which is greater than expected from the SOLPS-ITER simulation presented in this paper. This finding implies a potential lack of a transport mechanism in SOLPS-ITER or, perhaps, the diffusion coefficients used in the simulations are too low or spatially dependent. The latter concurs with other works using spatially varying transport coefficients to capture detached plasmas [35, 36, 37].

Following the high density region on the 2D maps in figure 4, the experimentally inferred density shows a continuation towards the outer target through the PFR. This continuation is consistent with the parallel transport along the field lines. Figure 6a) shows radial profiles across the outer divertor leg. These profiles also exhibit a radial shift of n_e towards the PFR that is very similar in both shape and values to the one observed in Figure 5a). However, the

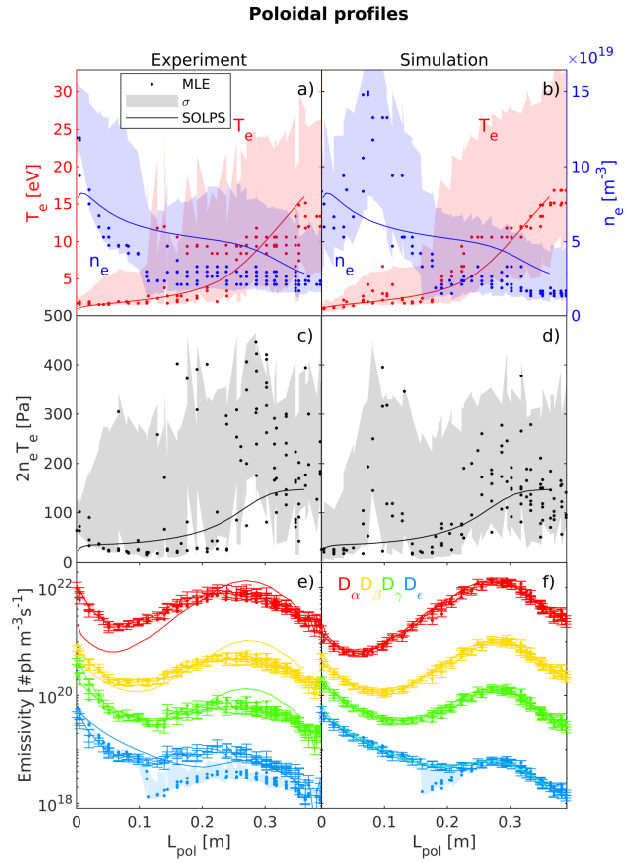


Figure 7. Poloidal profiles along the outer divertor leg as a function of distance to the outer target for $\rho_\psi = [1.01, 1.015]$: a) inferred density and temperature together with the SOLPS-ITER predictions; b) SOLPS prediction together with the synthetic emissivity analysis output; c) static pressure inferred from the experimental data; d) static pressure inferred from the synthetic emissivity; e) experimentally measured emissivity with 68% confidence interval of reconstructed emissivity (shaded regions mostly covered by the error bars) and SOLPS predictions (solid lines); f) Emissivities predicted by SOLPS (solid lines) together with the interpolated emissivity for synthetic testing and a 68% confidence interval of reconstructed emissivity. Location: magenta cells in Figure 1. TCV #63546, $t = 1.115$ s; SOLPS-ITER #150141.

density shift on the outer divertor leg could be only apparent due to a large density in the PFR. Although the analysis shows the density shift to the PFR, the SOLPS-ITER solution still falls within the uncertainty. Thus, from the density profile alone, it cannot be concluded whether the transport in the outer divertor leg is well captured by SOLPS-ITER. Nevertheless, when comparing the raw emissivity profiles in 6c) and 6d), one can note a shift of high- n Balmer lines to the PFR region in the experiment, which is not captured in the simulation.

More understanding of the analysis and its limitations can be gained from the profiles along the divertor leg. Figure 7 shows profiles for a selected

range of $\rho_\psi = [1.01, 1.015]$, along the outer divertor leg, up to the X-point. Unfortunately, the uncertainty of the analysis does not allow for the observation of small changes along the divertor leg. Instead, ballpark estimates of plasma parameters are obtained. Figures 7c) and 7d) show that the static plasma pressure inference obtained in this analysis with its uncertainties does not provide insights into the physics of edge plasmas. Raw emissivities in 7e) and 7f) show a significant increase of the low- n Balmer lines near the target to the values exceeding the peak value in the divertor leg. This increase is found with a much smaller magnitude in the SOLPS-ITER simulation.

5. Particle sources and sinks

In high recycling conditions, the divertor can be considered a closed system in which the ions arriving at the target are produced in the ionisation reactions within the divertor [40]. High recycling was previously observed spectroscopically at TCV with a line integrated measurement of the total ionisation I^{tot} matching the integrated saturation ion target current [7]. The analysis presented in this paper adds a 2D aspect to this measurement, yielding a flux-resolved profile.

The advantage of such a profile is the possibility of integration between the flux surfaces. In the high recycling regime, it predicts the ion target flux without accounting for any radial transport of ionised particles. This profile can be compared against the measured ion target flux to determine whether the zero radial transport assumption is valid. A

comparison between the integrated ionisation profiles can determine whether the particle source due to the electron-impact ionisation is well reproduced in SOLPS-ITER. The simulation results were processed using the ADAS model to compute the local ionisation rate for this comparison. Additionally, the simulation provides the particle flux at cell boundaries, which accounts for the transport of charged particles. Comparing the ionisation source, measured ion target flux, and the simulated particle flux at the cell boundaries can answer whether the radial particle transport in SOLPS-ITER captures the experiment.

Figure 8 compares the experimentally inferred ionisation and electron-ion recombination rate and its SOLPS-ITER counterparts. The inference shows an additional ionisation region at the target, which SOLPS-ITER does not capture. This region coincides with the electron temperatures in the range $\sim 1 - 4$ eV in Figure 4. At those temperatures, the plasma-molecule interaction can be a significant source of the $D_{3 \rightarrow 2}$ emission, which can be interpreted as ionisation [27, 28]. This contribution would not be accounted for in the ADAS model skewing the analysis results. This is discussed in detail in section 7.2.4. Fortunately, the 2D resolution of the MANTIS system allows for spatial separation of those regions. Therefore, the experimentally inferred ionisation rate will be separated between the divertor leg and the target. Those two regions will be considered separately to determine whether the target results are physical or a misinterpretation of the emission. This will be discussed in more detail in section 7.2.4.

The recombination rates shown in figures 8e)-8h) are insignificant when compared to the ionisation rates. This observation is consistent with the previous spectroscopic findings on TCV [7]. The recombination will be neglected as a particle sink in the remainder of this paper.

To obtain the ionisation profile for the inner and outer target, the inversion grid was split by a line drawn between the magnetic axis and the X-point. Then, the magnetic equilibrium was used to divide the SOL into ranges of ρ_ψ to select cells with centres within those ranges. To avoid numerical scatter as the ρ_ψ range approaches the analysis cell size, the analysis output polygon mesh was refined from 14549 cells to 128517 cells. Next, the volumes within those cells were toroidally integrated, and the total ionisation within each ρ_ψ range was divided by the machine floor area it intersects at the target.

Figure 9a) shows the particle balance for the inner target, the flux-resolved ionisation matches the integrated ionisation profile of the SOLPS-ITER, $\text{SOLPS-ITER}^{\text{tot}}$, while underestimating the total value. The measurements made by the Langmuir probes in the

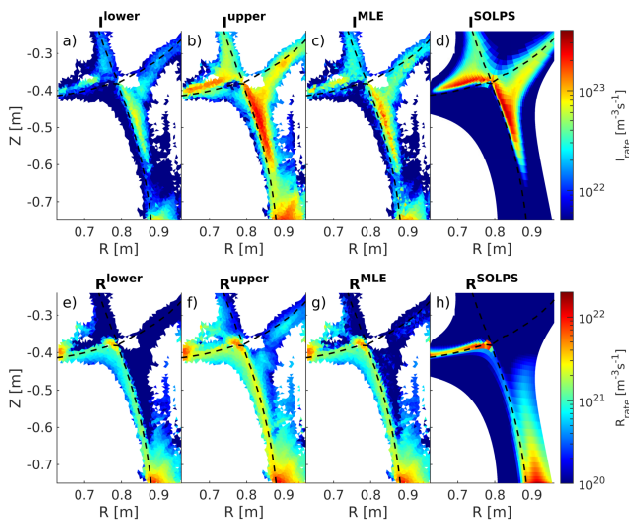


Figure 8. Comparison of the hydrogenic ionisation and recombination rates in the TCV divertor between the experiment and simulation. TCV #63546, $t = 1.115$ s; SOLPS-ITER #150141

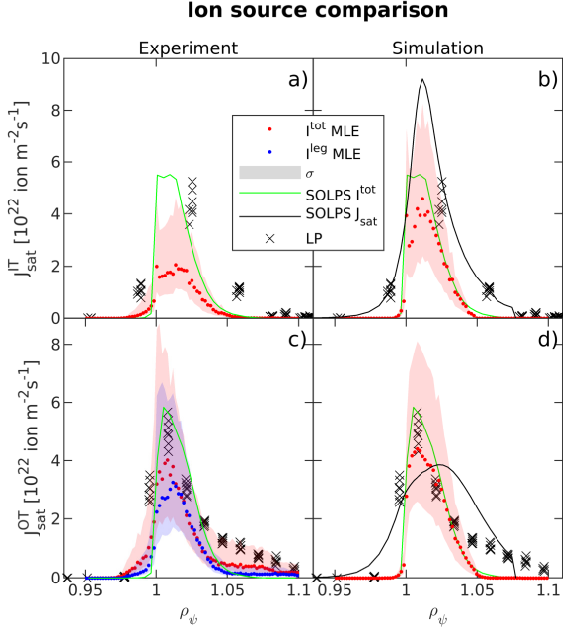


Figure 9. Ionisation source comparison between the experiment and the simulation, including synthetic testing on the simulation. a),c) Experimentally measured ionisation to the inner target and outer target respectively; b),d) SOLPS-ITER predicted ionisation and the ion saturation current accounting for transport to the inner and outer target respectively. TCV #63546, $t = 1.115$ s; SOLPS-ITER #150141.

far SOL at the inner target show a higher $J_{\text{sat}}^{\text{IT}}$ than expected from the ionisation, which does not account for transport. A comparison against the simulation in 9b) shows that the predicted SOLPS J_{sat} at the cell boundaries, which includes radial and poloidal particle transport, matches the values measured by the Langmuir probes. However, the probe coverage does not capture the peak of the profile; with only three probes, the match should be taken cautiously.

Figure 9c) presents the analysis results for the outer target. Since two ionisation regions are observed, the inference was also split at $Z = -0.65$ m forming two separate regions; the divertor leg, I^{leg} , which is captured by the SOLPS-ITER and the target, which is not. The I^{tot} presents the total ionisation in the outer divertor leg.

The shape and magnitude of the ionisation in the divertor leg, I^{leg} , are well captured by SOLPS-ITER. Simulated and measured ionisation in the divertor leg, I^{leg} , also matches the peak ion target flux measured by the Langmuir probes. *Since the sum of ionisation does not account for any radial transport of particles after the ionisation event, one can conclude that the radial transport is not necessary to explain the peak ion target flux to the outer target.*

Figure 9d), shows SOLPS J_{sat} , which is the ion flux at the cell boundaries at the target accounting

for the transport of charged particles in SOLPS-ITER. It does not match the experimentally derived target flux profile, which means that the radial transport of charged particles in the outer divertor leg is overestimated in SOLPS-ITER.

6. Time evolution of the discharge

The radial shift between density and temperature profile at the HFS promotes recombination in the locations where high density and low temperature overlap. Therefore, it can be easily observed and tracked in the inferred power radiated due to recombination P_{rec} in Figure 10. The figure shows a maximum near the X-point as time advances, the maximum and the size increase while stretching into a double lobe structure. In the final stage, the X-point lobe disappears. The remaining lobe creates an axisymmetric region of low temperature and high density. Its effects on the low-Z impurity emission can be observed in Figure 11 which presents total hydrogenic radiation losses $P_{\text{exc}} + P_{\text{rec}}$, the total radiated power measured by bolometry and the C III emissivity of the C^{2+} ion, which was previously found to be one of the main radiating species in the TCV edge plasmas [20]. As the blob develops, the impurity emission enters the confined region showing a poloidal asymmetry coinciding with the bolometric reconstruction. The characteristics of a poloidally asymmetric, increased density region on the HFS, combined with a relatively low temperature, are consistent with the description of a High Field Side MARFE [41]. Therefore, for the remainder of this paper, it will be referred to as a MARFE.

The MARFE movement can be tracked by

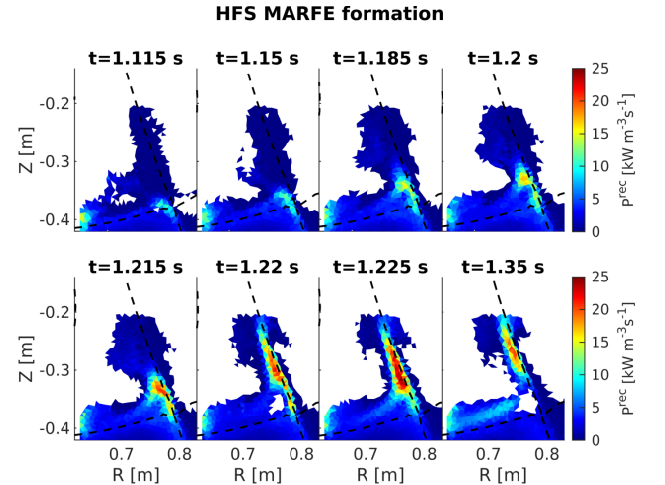


Figure 10. Time evolution of the Hight Field Side MARFE formation presented in the inferred Maximum Likelihood Estimate of power spent on hydrogenic recombination.

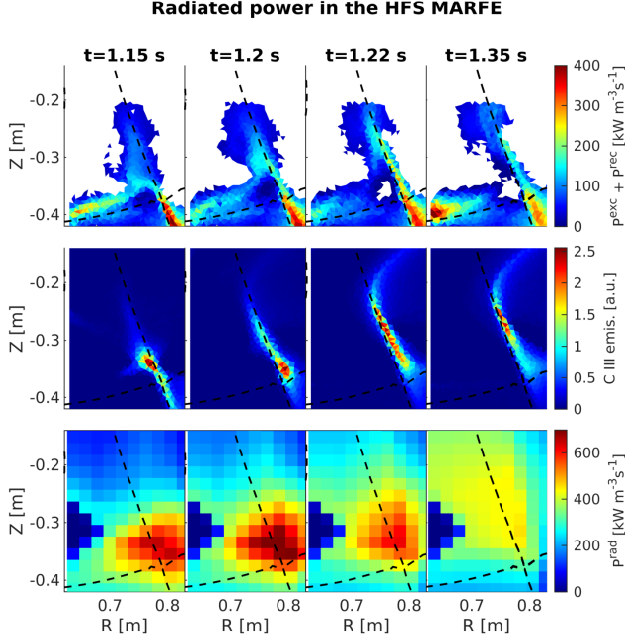


Figure 11. Time evolution of the High Field Side MARFE formation in total hydrogenic radiation losses, impurity emission and total radiated power measured with bolometry.

calculating the poloidal distance to the inner target, $L_{\text{pol}}^{\text{MARFE}}$ of the cell with the highest P_{rec} . Figure 12a) presents the tracking results together with the upstream pressure obtained through the analysis in section 3.3, and its smoothened version obtained through a moving mean of 3 points. The traces show that the MARFE formation coincides with a drop in the upstream pressure consistent with cooling the plasma edge.

To observe the effects of the MARFE formation on the ionisation in the divertor, the ionisation inference was separated into the divertor leg, $I_{\text{ot}}^{\text{leg}}$, and the divertor target, $I_{\text{ot}}^{\text{target}}$, the ionisation was split using a local minimum of D_{α} emission in the poloidal profile as presented in Figure 7e). At TCV, the impurity emission fronts using both tomographic and non-tomographic inversion methods are frequently used to compare discharges. Therefore, for reference, Figure 12b) presents this local emissivity minimum together with the C III emission front tracking using a non-tomographic method for reference [42].

The peak and total values of the inferred ionisation and the ion target flux measured by the Langmuir probes are presented in Figure 12c) and d) respectively. Interestingly, the separation between the two ionisation regions appears near the Γ^{peak} rollover.

Figure 12 shows that the peak particle flux rollover is also observed in the inferred peak ionisation in the divertor leg, $I_{\text{ot}}^{\text{leg}}$. The rollover coincides with the drop of the upstream pressure and the MARFE formation

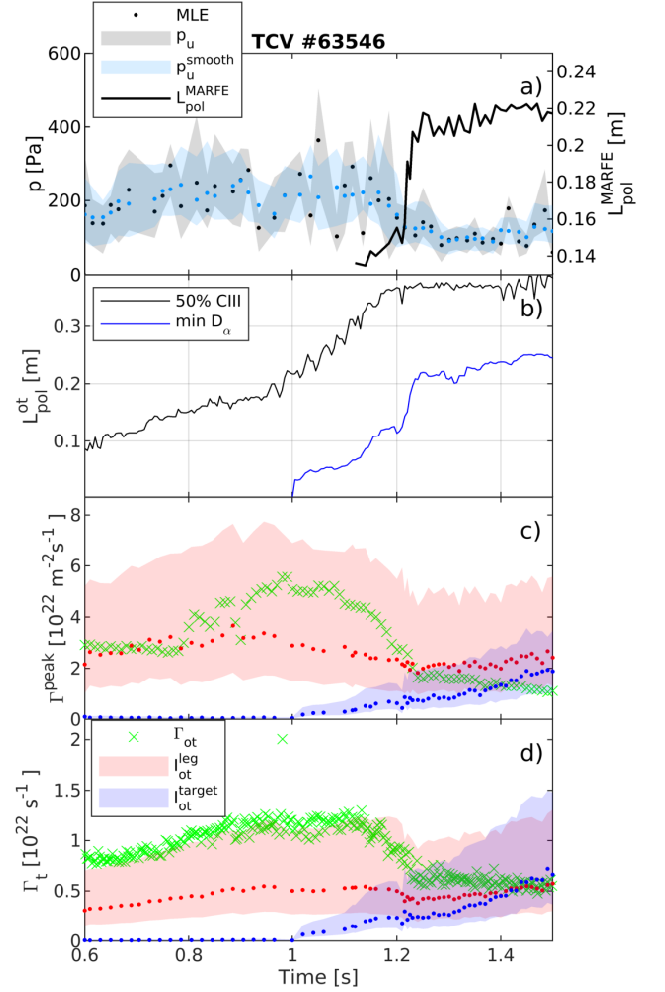


Figure 12. Time evolution of the relevant divertor parameters: a) inferred upstream pressure together with the distance of the MARFE to the target, b) impurity front location together with the minimum of D_{α} between the two ionisation regions, c) peak ion flux to the inner and outer targets measured by the Langmuir probes, d) total ion flux to the outer target measured by the Langmuir probes together with the spectroscopically inferred ionisation split between the divertor leg and the target regions. TCV #63546

in Fig. 12a). Once the MARFE is formed, the total ion target flux decreases by a factor of about 2, similar to the decrease of the upstream pressure.

The total inferred ionisation in the outer divertor leg, $I_{\text{ot}}^{\text{leg}}$ and the integrated ion flux are shown in Figure 12d). The $I_{\text{ot}}^{\text{leg}}$ coincides with the total ion target flux throughout the discharge. Adding the inferred ionisation at the target, $I_{\text{ot}}^{\text{target}}$ would result in more ions produced in the divertor leg than arriving at the target. A positive balance of ions in the divertor is possible; however, it would require plasma flow from the divertor leg to the core. Past the MARFE formation and the Γ_t rollover, both $I_{\text{ot}}^{\text{target}}$ and $I_{\text{ot}}^{\text{leg}}$ are found to be sufficiently high to maintain the high

recycling.

7. Discussion

7.1. Far SOL neutral density inference

Balmer line emissivities were used to solve the ADAS collisional-radiative model of hydrogen to infer plasma and neutral atomic density ranges together with the electron temperature. The solutions were used to match the experimentally obtained upstream profiles to their SOLPS-ITER counterparts. The matching showed a good agreement between electron temperature and density while revealing a significant difference in the neutral atomic density in the far SOL. Although the source of the mismatch is unclear, one could speculate that it is caused by the wall conditions in terms of recycling coefficients for neutral atoms in the simulation. This difference in the far SOL was not observed in other discharges at higher plasma currents, which could be due to narrower SOL, thus decreasing the interaction with the machine wall. More analysis of a broader range of experimental parameters is needed to conclude the source of this mismatch.

7.2. Sources of error

7.2.1. Incomplete localisation of the tomographic inversion

The emissivities used in this work were obtained using a tomographic inversion process, which may not be able to fully localise the emission along the lines of sight as seen by the camera. This deficiency results in parabolic streaks of light observed in figures 1 or 3a)-d). Consequently, in the outer divertor leg, the maximum intensity of the radial profiles can be underestimated. At the same time, both sides of the peak emission can be overestimated by spreading the emission in the far SOL and the PFR. On the inner divertor leg, the tomographic inversion process might displace the emission poloidally between the inner strike point and the X-point and radially to the PFR. The incomplete localisation contributes to the experimentally observed emission in the PFR and may contribute to the spreading in the radial profiles of n_e and T_e .

7.2.2. Machine wall reflections

The tomographic inversions used in this work do not account for tile reflection, which can also influence the reconstructions. Accounting for wall reflections is a common practice in metallic wall tokamaks [43, 44]. In TCV, the walls are covered with graphite tiles, which are expected to reflect significantly less light than polished metallic walls. A study of the effects of reflections in JET ITER-like, i.e. metallic wall,

found that reflections amplified the brightness by approximately 10% in the brightest regions. In the more remote parts of the image, 50 to 100% of the emission could be comprised of reflections [43].

7.2.3. Absolute calibration uncertainty

One of the biggest sources of uncertainty is the absolute calibration [24]. The interference filters' transmission curves are currently used in the calculations for the absolute calibration, resulting in an uncorrelated 12% systematic error for each camera. Correlating the error between the cameras would decrease the inference uncertainty.

7.2.4. Limitations of the plasma emission model

Recent works on TCV highlight the role of molecular reactions in the interpretation of the Balmer series of hydrogen with schemes of separating integrated emission into excitation, recombination, and the molecular contributions [27, 28]. This work adds a new aspect to it, a 2D spatial separation. In a 2D solution, one can spot regions that give unexpected results and investigate whether the assumptions behind the ADAS model used in this work still hold. One such region is found in the vicinity of the outer target, where the 2D map of ionisation rate in figure 8 shows a maximum near the target. The corresponding SOLPS-ITER simulation does not capture it. This observation raises whether it is an actual region ionisation or a misinterpretation of the emission due to plasma-molecule interactions.

Current modelling of the molecular contributions to the deuterium Balmer lines predicts that strong contributions to the emission spectrum would appear as excitation in plasma with temperatures 5–15 eV [27] which is not observed in figure 4. However, molecular contributions may also have different magnitudes, e.g. sufficient to skew the results but not dominant. Furthermore, depending on the magnitude, it could also increase the inferred electron temperature by a certain amount; for example, it could increase T_e from 2 to 4 eV.

The line ratio of $D_{4\rightarrow 2}$ to $D_{3\rightarrow 2}$ near the target reaches values of approximately 0.065. This ratio is consistent with the emission dominated by the plasma interaction with the H_2^+ molecule obtained through Yacora for TCV conditions in [27]. Furthermore, figure 3 shows a pattern of over and underestimation in the analysis residuals at the outer target. It could indicate that a solution consistent with all measured Balmer lines cannot be found in the ADAS model.

It is also worth investigating whether the value of the ionisation at the target is plausible. The integrated ionisation in figure 9c) shows a good agreement between the ionisation near the target and

the ion saturation current profile in the far SOL, $\rho_\psi = [1.05, 1.1]$. It could result from the inversion error due to the reflections from the outer target. Misplaced light along the line of sight due to the incomplete localisation could also broaden the target profile. A good example of this inversion artefact can be found in figure 8b), where the ionisation forms a triangular shape near the floor at $R = 0.9$ m. The total ionisation in figure 12 exceeds the saturation ion target current by a factor of 2. Unless there are significant plasma sinks other than the target currents, assuming 1 m^3 of plasma, with the excess ionisation of $5 \cdot 10^{21} \text{ s}^{-1}$, the average plasma density would increase by 10^{20} m^{-3} every 20 ms. This is not the case in the experiment.

The arguments presented in the section strongly suggest that the hydrogen emission at the target is dominated by the plasma-molecule interaction, which cannot be neglected in the analysis of the Balmer line series. Detailed investigations are critical since the 2D maps of n_e and T_e in figure 4 do not exhibit clear unphysical behaviour such as an increase of T_e towards the divertor targets.

7.3. Role of the X-point potential well in the HFS MARFE formation

As the line average density increases, a low temperature and high density region forms on the HFS, consistent with the radial $E \times B$ drift captured by SOLPS-ITER. This region coincides with the maximum emission of C^{2+} ions and bolometric radiation in figure 11. It could be caused by an accumulation of carbon on the HFS; n_e , T_e conditions promoting radiation, or a combination of those. Either way, it leads to a strongly radiating region on the HFS. The hydrogenic recombination maximum of this region has a structure which is shown in figure 10. The region stretches into two lobes before one moves poloidally upward, leading to a MARFE formation. This lobe separation could be a crossing in the impurity cooling curve, beyond which the radiated power increases with decreasing electron temperature. It would act as a positive feedback loop, further decreasing the local temperature. As a result, one of the lobes would have an increased cooling capability, consistent with the upstream electron temperature collapse as it moves upstream. The temperature collapse results in the upstream pressure collapse shown in figure 12a).

Combining those observations, one can argue that the $E \times B$ radial transport on the HFS induced by the X-point potential well creates conditions for a MARFE-seed; once the seed reaches the right conditions, the HFS MARFE forms. Then, it collapses the upstream electron temperature, which causes the upstream pressure drop resulting in a symmetric ion target current rollover on both targets. Alternatively,

the movement could start with a change of upstream conditions, which triggers the MARFE formation by dropping the upstream T_e . In both of those explanations, the X-point potential well acts as a seed for the HFS MARFE.

8. Summary and outlook

Multispectral imaging was used to measure the emissivity of the Balmer series of deuterium. The emissivities were used with the ADAS collisional-radiative model of hydrogen to infer ranges of the neutral atomic density together with the electron density and temperature. Simultaneously, a SOLPS-ITER simulation was used to generate synthetic data to verify the implementation of the analysis while comparing the profiles of plasma parameters to the experiment.

Experimental observations are consistent with an $E \times B$ -induced radial shift between density and temperature at the inner divertor leg predicted by SOLPS-ITER. The plasma density profile continued through the separatrix to the PFR smoothly. Thus, showing a significant cross-field particle transport through the separatrix that is not captured by the SOLPS-ITER simulation. The radial profiles across the outer divertor leg showed an analogous increase of density in the PFR consistent with the parallel particle transport.

The origins of a MARFE presented in this paper can be traced to the existence of this $E \times B$ drift caused by the X-point potential well. As the line average density increases, the low temperature and high density region on the HFS stretch into two lobes. One of them evolves into the HFS MARFE. This evolution coincides with the upstream pressure loss leading to a symmetric rollover of the ion target flux, which can be interpreted as detachment. However, it does not necessarily mean that detachment was achieved. The ion target flux can be reduced by radiation alone, which one would call SOL power starvation. Detachment additionally requires a large pressure drop along the field lines towards the target, which could not be recovered in this analysis as shown in figure 7c) and d).

An unexpected ionisation region near the outer target was found. Upon closer investigation, the region appears to be consistent with hydrogen Balmer emission due to plasma-molecule interaction, not included in the ADAS model.

The rollover was also observed in the inferred ionisation in the divertor leg. Thus, potentially provides optical tracking of the peak particle flux to the outer divertor target. This inference provides a wealth of information for the power exhaust control efforts. Current control schemes involve either the control

of radiation that does not provide the information about the peak target fluxes [45, 46, 47, 48, 49] or control of the target quantities through probes or shunt currents, which do not provide the information about the plasma edge [50, 51, 52, 53, 54]. The analysis presented in this paper links the particle sources and sinks between the upstream location and the target. Thus, simultaneously providing valuable information about the state of the divertor along and across the SOL.

The power balance needs to be added for a complete view of the SOL. This analysis should be extended with impurity models to provide input for the SOL power balance due to impurity radiation. Such an addition would allow for Multiple Input, Multiple Output (MIMO) control. Different gas valves would be actuated independently to seed impurities affecting the power balance or increase the divertor neutral pressure through fueling. Furthermore, including helium spectroscopy and accounting for the emission due to plasma-molecule interaction would improve the inference. Ultimately, this analysis would have to be performed in real-time within a fraction of a second, which would require speed-up by 4-5 orders of magnitude from its current 2600s per time step on a single CPU. Such a performance improvement is not inconceivable when employing physics informed neural networks that already delivered 3-5 orders of magnitude speed-up by approximating a quasilinear turbulence model QuaLiKiz [55].

Acknowledgments

This work has been carried out within the framework of the EUROfusion Consortium, funded by the European Union via the Euratom Research and Training Programme (Grant Agreement No 101052200 — EUROfusion). Views and opinions expressed are however those of the author(s) only and do not necessarily reflect those of the European Union or the European Commission. Neither the European Union nor the European Commission can be held responsible for them. This work was supported in part by the Swiss National Science Foundation. The views and opinions expressed herein do not necessarily reflect those of the ITER Organization.

References

- [1] N. J. Lopes Cardozo, A. G.G. Lange, and G. J. Kramer. Fusion: Expensive and Taking Forever? *Journal of Fusion Energy*, 35(1):94–101, 2016.
- [2] A. J. Creely, M. J. Greenwald, S. B. Ballinger, D. Brunner, J. Canik, J. Doody, T. Fülöp, D. T. Garnier, R. Granetz, T. K. Gray, C. Holland, N. T. Howard, J. W. Hughes, J. H. Irby, V. A. Izzo, G. J. Kramer, A. Q. Kuang, B. Labombard, Y. Lin, B. Lipschultz, N. C. Logan, J. D. Lore, E. S. Marmar, K. Montes, R. T. Mumgaard, C. Paz-Soldan, C. Rea, M. L. Reinke, P. Rodriguez-Fernandez, K. Särkimäki, F. Sciortino, S. D. Scott, A. Snicker, P. B. Snyder, B. N. Sorbom, R. Sweeney, R. A. Tinguely, E. A. Tolman, M. Umansky, O. Vallhagen, J. Varje, D. G. Whyte, J. C. Wright, S. J. Wukitch, and J. Zhu. Overview of the SPARC tokamak. *Journal of Plasma Physics*, 86(5):865860502, 2020.
- [3] T. Eich, A. W. Leonard, R. A. Pitts, W. Fundamenski, R. J. Goldston, T. K. Gray, A. Herrmann, A. Kirk, A. Kallenbach, O. Kardaun, A. S. Kukushkin, B. Labombard, R. Maingi, M. A. Makowski, A. Scarabosio, B. Sieglin, J. Terry, and A. Thornton. Scaling of the tokamak near the scrape-off layer H-mode power width and implications for ITER. *Nuclear Fusion*, 53(9):093031, 2013.
- [4] N. Christen, C. Theiler, T. D. Rognlien, M. E. Rensink, H. Reimerdes, R. Maurizio, and B. Labit. Exploring drift effects in TCV single-null plasmas with the UEDGE code. *Plasma Physics and Controlled Fusion*, 59(10):105004, 2017.
- [5] A. Fil, B. Lipschultz, D. Moulton, B. D. Dudson, O. Février, O. Myatra, C. Theiler, K. Verhaegh, and M. Wensing. Separating the roles of magnetic topology and neutral trapping in modifying the detachment threshold for TCV. *Plasma Physics and Controlled Fusion*, 62(3):035008, 2020.
- [6] M. Wensing, B. P. Duval, O. Février, A. Fil, D. Galassi, E. Havlickova, A. Pereh, H. Reimerdes, C. Theiler, K. Verhaegh, and M. Wischmeier. SOLPS-ITER simulations of the TCV divertor upgrade. *Plasma Physics and Controlled Fusion*, 61(8):085029, 2019.
- [7] K. Verhaegh, B. Lipschultz, B. P. Duval, A. Fil, M. Wensing, C. Bowman, and D. S. Gahle. Novel inferences of ionisation and recombination for particle/power balance during detached discharges using deuterium Balmer line spectroscopy. *Plasma Physics and Controlled Fusion*, 61(12):125018, 2019.
- [8] C. Bowman, J. R. Harrison, B. Lipschultz, S. Orchard, K. J. Gibson, M. Carr, K. Verhaegh, and O. Myatra. Development and simulation of multi-diagnostic Bayesian analysis for 2D inference of divertor plasma characteristics. *Plasma Physics and Controlled Fusion*, 62(4):045014, 2020.
- [9] K. Verhaegh, B. Lipschultz, B.P. Duval, O. Février, A. Fil, C. Theiler, M. Wensing, C. Bowman, D.S. Gahle, J.R. Harrison, B. Labit, C. Marini, R. Maurizio, H. de Oliveira, H. Reimerdes, U. Sheikh, C.K. Tsui, N. Vianello, and W.A.J. Vijvers. An improved understanding of the roles of atomic processes and power balance in divertor target ion current loss during detachment. *Nuclear Fusion*, 59(12):126038, 2019.
- [10] A. Loarte, B. Lipschultz, A. S. Kukushkin, G. F. Matthews, P. C. Stangeby, N. Asakura, G. F. Counsell, G. Federici, A. Kallenbach, K. Krieger, A. Mahdavi, V. Philipps, D. Reiter, J. Roth, J. Strachan, D. Whyte, R. Doerner, T. Eich, W. Fundamenski, A. Herrmann, M. Fenstermacher, P. Ghendrih, M. Groth, A. Kirschner, S. Konoshima, B. Labombard, P. Lang, A. W. Leonard, P. Monier-Garbet, R. Neu, H. Pacher, B. Pegourie, R. A. Pitts, S. Takamura, J. Terry, and E. Tsitrone. Chapter 4: Power and particle control. *Nuclear Fusion*, 47(6):S203, 2007.
- [11] R.A. Pitts, X. Bonnin, F. Escourbiac, H. Frerichs, J.P. Gunn, T. Hirai, A.S. Kukushkin, E. Kaveeva, M.A. Miller, D. Moulton, V. Rozhansky, I. Senichenkov, E. Sytova, O. Schmitz, P.C. Stangeby, G. De Temmerman, I. Veselova, and S. Wiesen. Physics basis for the first iter tungsten divertor. *Nuclear Materials and Energy*, 20:100696, 2019.
- [12] D. Maisonnier, D. Campbell, I. Cook, L. Di Pace,

- L. Giancarli, J. Hayward, A. Li Puma, M. Medrano, P. Norajitra, M. Roccella, P. Sardain, M. Q. Tran, and D. Ward. Power plant conceptual studies in Europe. *Nuclear Fusion*, 47(11):1524–1532, 2007.
- [13] H. Reimerdes, B. P. Duval, J. R. Harrison, B. Labit, B. Lipschultz, T. Lunt, C. Theiler, C. K. Tsui, K. Verhaegh, W. A. J. Vijvers, J. A. Boedo, G. Calabro, F. Crisanti, P. Innocente, R. Maurizio, V. Pericoli, U. Sheikh, M. Spolare, and N. Vianello. TCV experiments towards the development of a plasma exhaust solution. *Nuclear Fusion*, 57(12):126007, 2017.
- [14] H. Reimerdes, B. P. Duval, H. Elaian, A. Fasoli, O. Février, C. Theiler, F. Bagnato, M. Baquero-Ruiz, P. Blanchard, D. Brida, C. Colandrea, H. de Oliveira, D. Galassi, S. Gorno, S. Henderson, M. Komm, B. Linehan, L. Martinelli, R. Maurizio, J. M. Moret, A. Perek, H. Raj, U. Sheikh, D. Testa, M. Toussaint, C. K. Tsui, and M. Wensing. Initial TCV operation with a baffled divertor. *Nuclear Fusion*, 61(2):024002, 2021.
- [15] A. Fasoli, H. Reimerdes, Alberti S., M. Baquero, B. P. Duval, E. Havlikova, A. Karpushov, J.-M. Moret, M. Toussaint, H. Elaian, M. Silva, C. Theiler, D. Vaccaro, and the TCV team. Tcv heating and divertor upgrades. *Nuclear Fusion*, 60(1):016019, 2020.
- [16] O. Février, H. Reimerdes, C. Theiler, D. Brida, C. Colandrea, H. De Oliveira, B. P. Duval, D. Galassi, S. Gorno, S. Henderson, M. Komm, B. Labit, B. Linehan, L. Martinelli, A. Perek, H. Raj, U. Sheikh, C. K. Tsui, and M. Wensing. Divertor closure effects on the TCV boundary plasma. *Nuclear Materials and Energy*, 27:100977, 2021.
- [17] S. Wiesen, D. Reiter, V. Kotov, M. Baelmans, W. Dekeyser, A. S. Kukushkin, S. W. Lisgo, R. A. Pitts, V. Rozhansky, G. Saibene, I. Veselova, and S. Voskoboynikov. The new SOLPS-ITER code package. *Journal of Nuclear Materials*, 463:480–484, 2015.
- [18] X. Bonnin, W. Dekeyser, R. A. Pitts, D. Coster, S. Voskoboynikov, and S. Wiesen. Presentation of the New SOLPS-ITER Code Package for Tokamak Plasma Edge Modelling. *Plasma and Fusion Research*, 11:1403102, 2016.
- [19] M. Wensing, J. Loizu, H. Reimerdes, B. P. Duval, M. Wischmeier, and the TCV team. X-point potential well formation in diverted tokamaks with unfavorable magnetic field direction. *Nuclear Fusion*, 60(5):054005, 2020.
- [20] M. Wensing. *Drift-related transport and plasma-neutral interaction in the TCV divertor*. PhD thesis, École polytechnique fédérale de Lausanne, February 2021.
- [21] J. Karhunen, B. Lomanowski, V. Solokha, S. Aleiferis, P. Carvalho, M. Groth, H. Kumpulainen, K. D. Lawson, A. G. Meigs, and A. Shaw. Estimation of 2d distributions of electron density and temperature in the jet divertor from tomographic reconstructions of deuterium balmer line emission. *Nuclear Materials and Energy*, 25:100831, 2020.
- [22] A. Huber, S. Brezinsek, Ph. Mertens, B. Schweer, G. Sergienko, A. Terra, G. Arnoux, N. Balshaw, M. Clever, T. Edlingdon, S. Egner, J. Farthing, M. Hartl, L. Horton, D. Kampf, J. Klammer, H. T. Lambertz, G. F. Matthews, C. Morlock, A. Murari, M. Reindl, V. Riccardo, U. Samm, S. Sanders, M. Stamp, J. Williams, K. D. Zastrow, and C. Zauner. Development of a mirror-based endoscope for divertor spectroscopy on jet with the new iter-like wall (invited). *Review of Scientific Instruments*, 83(10):10D511, 2012.
- [23] J. Karhunen, B. Lomanowski, V. Solokha, S. Aleiferis, P. Carvalho, M. Groth, K. D. Lawson, A. G. Meigs, and A. Shaw. Assessment of filtered cameras for quantitative 2d analysis of divertor conditions during detachment in JET l-mode plasmas. *Plasma Physics and Controlled Fusion*, 63(8):085018, 2021.
- [24] A. Perek, B. L. Linehan, M. Wensing, K. Verhaegh, I. G. J. Classen, B. P. Duval, O. Février, H. Reimerdes, C. Theiler, T. A. Wijkamp, and M. R. de Baar. Measurement of the 2D emission profiles of hydrogen and impurity ions in the TCV divertor. *Nuclear Materials and Energy*, 26(2021):100858, 2021.
- [25] A. Perek, W. A. J. Vijvers, Y. Andrebe, I. G. J. Classen, B. P. Duval, C. Galperti, J. R. Harrison, B. L. Linehan, T. Ravensbergen, K. Verhaegh, and M. R. de Baar. Mantis: A real-time quantitative multispectral imaging system for fusion plasmas. *Review of Scientific Instruments*, 90(12):123514, 2019.
- [26] M. O’Mullane H. Summers. Atomic data and analysis structure. Technical Report JET-P9735, 2000.
- [27] K. Verhaegh, B. Lipschultz, C. Bowman, B. P. Duval, U. Fantz, A. Fil, J. R. Harrison, D. Moulton, O. Myatra, D. Wunderlich, F. Federici, D. S. Gahle, A. Perek, and M. Wensing. A novel hydrogenic spectroscopic technique for inferring the role of plasma-molecule interaction on power and particle balance during detached conditions. *Plasma Physics and Controlled Fusion*, 63(3):035018, 2021.
- [28] K. Verhaegh, B. Lipschultz, J. Harrison, B. Duval, C. Bowman, A. Fil, D. S. Gahle, D. Moulton, O. Myatra, A. Perek, C. Theiler, and M. Wensing. A study of the influence of plasma-molecule interactions on particle balance during detachment. *Nuclear Materials and Energy*, 26:100922, 2021.
- [29] K. Verhaegh, B. Lipschultz, J. R. Harrison, B. P. Duval, A. Fil, M. Wensing, C. Bowman, D. S. Gahle, A. S. Kukushkin, D. Moulton, A. Perek, A. Pshenov, F. Federici, O. Février, O. Myatra, A. J. Smolders, and C. Theiler. The role of plasma-molecule interactions on power and particle balance during detachment on the TCV tokamak. *Nuclear Fusion*, 61(10):106014, 2021.
- [30] Z. I. Botev, J. F. Grotowski, and D. P. Kroese. Kernel density estimation via diffusion. *Annals of Statistics*, 38(5):2916–2957, 2010.
- [31] A. L. Moser, A. W. Leonard, A. G. McLean, H. Q. Wang, and J. G. Watkins. The effect of divertor closure on detachment onset in DIII-D. *Nuclear Materials and Energy*, 19:67–71, 2019.
- [32] M. Wensing, H. Reimerdes, O. Février, C. Colandrea, L. Martinelli, K. Verhaegh, F. Bagnato, P. Blanchard, B. Vincent, A. Perek, S. Gorno, H. de Oliveira, C. Theiler, B. P. Duval, C. K. Tsui, M. Baquero-Ruiz, and M. Wischmeier. SOLPS-ITER validation with TCV L-mode discharges. *Physics of Plasmas*, 28(8):082508, 2021.
- [33] A. E. Jaervinen, S. L. Allen, M. Groth, A. G. McLean, T. D. Rognlien, C. M. Samuelli, A. Briesemeister, M. Fenstermacher, D. N. Hill, A. W. Leonard, and G. D. Porter. Interpretations of the impact of cross-field drifts on divertor flows in DIII-D with UEDGE. *Nuclear Materials and Energy*, 12:1136–1140, 2017.
- [34] L. Aho-Mantila, S. Potzel, D. P. Coster, M. Wischmeier, M. Brix, R. Fischer, S. Marsen, A. Meigs, H. W. Müller, A. Scarabosio, M. F. Stamp, S. Brezinsek, and The ASDEX Upgrade Team. Assessment of solps5.0 divertor solutions with drifts and currents against l-mode experiments in asdex upgrade and jet. *Plasma Physics and Controlled Fusion*, 59(3):035003, 2017.
- [35] F. Reimold, M. Wischmeier, S. Potzel, L. Guimaraes, D. Reiter, M. Bernert, M. Dunne, and T. Lunt. The high field side high density region in SOLPS-modeling of nitrogen-seeded H-modes in ASDEX Upgrade. *Nuclear Materials and Energy*, 12:193–199, 2017.
- [36] J. Karhunen, M. Groth, D. P. Coster, D. Carralero,

- L. Guimaraes, V. Nikolaeva, S. Potzel, T. Pütterich, F. Reimold, A. Scarabosio, E. Viezzer, and M. Wischmeier. Solps 5.0 simulations of the high-field side divertor detachment of l-mode plasmas in asdex upgrade with convection-dominated radial sol transport. *Nuclear Materials and Energy*, 19:279–286, 2019.
- [37] H. Wu, F. Subba, M. Wischmeier, M. Cavedon, and R. Zanino. Solps-iter modeling of asdex upgrade l-mode detachment states. *Plasma Physics and Controlled Fusion*, 63(10):105005, 2021.
- [38] H. De Oliveira, P. Marmillod, C. Theiler, R. Chavan, O. Février, B. Labit, P. Lavanchy, B. Marlétaz, and R. A. Pitts. Langmuir probe electronics upgrade on the tokamak à configuration variable. *Review of Scientific Instruments*, 90(8):083502, 2019.
- [39] M. Wensing, H. de Oliveira, J. Loizu, C. Colandrea, O. Février, S. Gorno, H. Reimerdes, C. Theiler, A. Smolders, B. P. Duval, C. K. Tsui, M. Wischmeier, D. Brida, S. Henderson, and M. Komm. Experimental verification of X-point potential well formation in unfavorable magnetic field direction. *Nuclear Materials and Energy*, 25:100839, 2020.
- [40] P. C. Stangeby. Basic physical processes and reduced models for plasma detachment. *Plasma Physics and Controlled Fusion*, 60(4):044022, 2018.
- [41] B. Lipschultz. Review of MARFE phenomena in tokamaks. *Journal of Nuclear Materials*, 145-147(C):15–25, 1987.
- [42] T. Ravensbergen, M. Van Berkel, S. A. Silburn, J. R. Harrison, A. Perek, K. Verhaegh, W. A.J. Vijvers, C. Theiler, A. Kirk, M. R. De Baar, The Eurofusion Mst1 Team, and The Tcv Team. Development of a real-time algorithm for detection of the divertor detachment radiation front using multi-spectral imaging. *Nuclear Fusion*, 60(6):066017, 2020.
- [43] J. Karhunen, M. Carr, J. R. Harrison, B. Lomanowski, I. Balboa, P. Carvalho, M. Groth, A. Huber, G. F. Matthews, A. Meakins, and S. Silburn. Effect of reflections on 2D tomographic reconstructions of filtered cameras and on interpreting spectroscopic measurements in the JET ITER-like wall divertor. *Review of Scientific Instruments*, 90(10):103504, 2019.
- [44] M. Carr, A. Meakins, S. A. Silburn, J. Karhunen, M. Bernert, C. Bowman, A. Callarelli, P. Carvalho, C. Giroud, J. R. Harrison, S. S. Henderson, A. Huber, B. Lipschultz, T. Lunt, D. Moulton, and F. Reimold. Physically principled reflection models applied to filtered camera imaging inversions in metal walled fusion machines. *Review of Scientific Instruments*, 90(4):043504, 2019.
- [45] A. Kallenbach, M. Bernert, T. Eich, J.C. Fuchs, L. Giannone, A. Herrmann, J. Schweinzer, and W. Treutterer. Optimized tokamak power exhaust with double radiative feedback in ASDEX Upgrade. *Nuclear Fusion*, 52(12):122003, 2012.
- [46] D. Eldon, E. Kolemen, D. A. Humphreys, A. W. Hyatt, A. E. Järvinen, A. W. Leonard, A. G. McLean, A. L. Moser, T. W. Petrie, and M. L. Walker. Advances in radiated power control at DIII-D. *Nuclear Materials and Energy*, 18:285–290, 2019.
- [47] T. Ravensbergen, M. van Berkel, A. Perek, C. Galperti, B.P. Duval, O. Fevrier, R.J.R. van Kampen, F. Felici, J.T. Lammers, C. Theiler, Johan Schoukens, B. Linehan, M. Komm, S. Henderson, D. Brida, and M.R. de Baar. Real-time feedback control of the impurity emission front in tokamak divertor plasmas. *Nature Energy*, 12(1105), 2021.
- [48] G. S. Xu, Q. P. Yuan, K. D. Li, L. Wang, J. C. Xu, Q. Q. Yang, Y. M. Duan, L. Y. Meng, Z. S. Yang, F. Ding, J. B. Liu, H. Y. Guo, H. Q. Wang, D. Eldon, Y. Q. Tao, K. Wu, N. Yan, R. Ding, Y. F. Wang, Y. Ye, L. Zhang, T. Zhang, Q. Zang, Y. Y. Li, H. Q. Liu, G. Z. Jia, X. J. Liu, H. Si, E. Z. Li, L. Zeng, J. P. Qian, S. Y. Lin, L. Q. Xu, H. H. Wang, X. Z. Gong, and B. N. Wan. Divertor impurity seeding with a new feedback control scheme for maintaining good core confinement in grassy-ELM H-mode regime with tungsten monoblock divertor in EAST. *Nuclear Fusion*, 60(8):086001, 2020.
- [49] M. Bernert, F. Janky, B. Sieglin, A. Kallenbach, B. Lipschultz, F. Reimold, M. Wischmeier, M. Cavedon, P. David, M. G. Dunne, M. Griener, O. Kudlacek, R. M. McDermott, W. Treutterer, E. Wolfrum, D. Brida, O. Février, S. Henderson, and M. Komm. X-point radiation, its control and an ELM suppressed radiating regime at the ASDEX Upgrade tokamak. *Nuclear Fusion*, 61(2):024001, 2021.
- [50] A. Kallenbach, R. Dux, J.C. Fuchs, R. Fischer, B. Geiger, L. Giannone, A. Herrmann, T. Lunt, V. Mertens, R.M. McDermott, R. Neu, T. Putterich, S. Rathgeber, V. Rohde, K. Schmid, J. Schweinzer, and W. Treutterer. Divertor power load feedback with nitrogen seeding in ASDEX Upgrade. *Plasma Physics and Controlled Fusion*, 52(5):055002, 2010.
- [51] C. Guillemaut, M. Lennholm, J. Harrison, I. Carvalho, D. Valcarcel, R. Felton, S. Griph, C. Hogben, R. Lucock, G. F. Matthews, C. Perez Von Thun, R. A. Pitts, and S. Wiesen. Real-time control of divertor detachment in H-mode with impurity seeding using Langmuir probe feedback in JET-ITER-like wall. *Plasma Physics and Controlled Fusion*, 59(4):045001, 2017.
- [52] I. Khodunov, M. Komm, A. Havranek, J. Adamek, J. Cavalier, A. Devitre, M. Dimitrova, S. Elmore, M. Faitsch, P. Hacek, M. Imrisek, J. Krbec, M. Peterka, R. Panek, M. Tomes, K. Tomova, P. Vondracek, V. Weinzettl, Max-planck-institut Plasmaphysik, Garching Munchen, and De Lorraine. Real-time feedback system for divertor heat flux control at COMPASS tokamak. *Plasma Physics and Controlled Fusion*, 63(6):065012, 2021.
- [53] D. Brunner, W. Burke, A. Q. Kuang, B. Labombard, B. Lipschultz, and S. Wolfe. Feedback system for divertor impurity seeding based on real-time measurements of surface heat flux in the Alcator C-Mod tokamak. *Review of Scientific Instruments*, 87(2):023504, 2016.
- [54] D. Eldon, E. Kolemen, J. L. Barton, A. R. Briesemeister, D. A. Humphreys, A. W. Leonard, R. Maingi, M. A. Makowski, A. G. McLean, A. L. Moser, and P. C. Stangeby. Controlling marginally detached divertor plasmas. *Nuclear Fusion*, 57(6):066039, 2017.
- [55] K. L. Van De Plassche, J. Citrin, C. Bourdelle, Y. Camenen, F. J. Casson, V. I. Dagnelie, F. Felici, A. Ho, and S. Van Mulders. Fast modeling of turbulent transport in fusion plasmas using neural networks. *Physics of Plasmas*, 27(2):022310, 2020.